九州大学学術情報リポジトリ
Kyushu University Institutional Repository

Experimental and Numerical Study of a Wet-Towing System for Multi-Bucket Jacket Wind Turbines Considering Air Compressibility in Suction Caissons

Zhu, Hongzhong
Research Institute for Applied Mechanics, Kyushu University

Hu, Changhong
Research Institute for Applied Mechanics, Kyushu University

Watanabe, Seiya
Research Institute for Applied Mechanics, Kyushu University

Sueyoshi, Makoto
FREGATA TECH LLC

他

https://hdl.handle.net/2324/7362163

出版情報：Ocean Engineering. 336, 2025-06-13. Elsevier
バージョン：
権利関係：© 2025 The Authors. Published by Elsevier Ltd.

KYUSHU UNIVERSITY

Ocean Engineering 336 (2025) 121740

Contents lists available at ScienceDirect

Ocean Engineering

journal homepage: www.elsevier.com/locate/oceaneng

Research paper

Experimental and numerical study of a wet-towing system for multi-bucket jacket wind turbines considering air compressibility in suction caissons

Hongzhong Zhu [a,*], Changhong Hu [a], Seiya Watanabe [a], Makoto Sueyoshi [b], Rikizo Yamashita [c], Yoshihiro Matsuoka [c]

[a] Research Institute for Applied Mechanics, Kyushu University, Kasuga-Koen 6-1, Kasuga, 816-8580, Fukuoka, Japan
[b] FREGATA TECH LLC, 2340-1, Buzen, Fukuoka, 828-0066, Japan
[c] Civil Engineering Technology Division, Obayashi Corporation, 2-15-2, Konan, Minato-ku, Tokyo, 108-8502, Japan

ARTICLE INFO

Keywords:
Wet towing system
Wave basin tests
Unified seakeeping and maneuvering model
Multi-bucket jacket foundation
Damping coefficients identification
Air compressibility in caissons

ABSTRACT

Offshore wind energy is widely regarded as a promising solution for achieving global net-zero emissions, with wind turbine installations progressively expanding into far-offshore regions. The jacket foundation with multiple suction buckets has emerged as a feasible option for deep-water applications due to its ease of installation and retrieval. To reduce offshore transportation costs, this paper studies a novel wet-towing approach, in which a supplementary floater is employed to enhance the stability of the foundation during towing. Firstly, a prototype of the towing system and a 1:67.5 scale experimental model are developed. A series of experiments, including free-decay tests, regular wave response tests, and towing tests, are conducted to examine the hydrodynamic behavior of the system. Then, a numerical model is established to integrate seakeeping and maneuvering theories and incorporate the effects of air compressibility within the caissons to simulate the dynamic response of the towing system under various sea conditions. To improve model fidelity, linear and nonlinear damping coefficients are estimated based on experimental data. Numerical results show good agreement with experimental observations in most cases. The results further indicate that the presence of compressible air in the caissons increases the natural periods in heave and pitch by approximately 3.5 %, while the heave damping is reduced by 16 % and the pitch damping is increased by 25 %. Finally, the performance of the towing system is evaluated under a circular route, accounting for realistic met-ocean conditions.

1. Introduction

With growing social acceptance, maturing technologies, and the development of supply chains, offshore wind turbines (OWTs) are increasingly being seen as a promising solution to address carbon neutrality by the mid-century. In the past decade, offshore wind turbines have gradually moved from near-shore zones to far-offshore areas, raising new challenges in technical and economic feasibility (Díaz and Soares, 2020; McCoy et al., 2024). Recently, jacket structures combined with suction buckets, with their advantages of low construction cost, less environmental effects, ease of installation and retrieval, and adaptability to deep water, have attracted a great deal of attention (Shonberg et al., 2017; Bagheri et al., 2019; Lian et al., 2022; Zhang et al., 2022; Wei et al., 2025; Li et al., 2024; Grecu et al., 2024).

To install a bottom-fixed offshore wind turbine, its components are usually loaded in advance onto a self-elevating platform (SEP) vessel at port and transported to the wind farm site. The SEP vessel then lifts itself out from the sea surface by penetrating its legs into the seabed, avoiding the effects of ocean waves and ensuring its stability during operation. Cranes are used lastly to install foundations and wind turbines (Díaz and Soares, 2020). Due to the high cost and the shortage of large SEP vessels, the massive installation of offshore wind turbines is challenging. To reduce the dependence of offshore wind on heavy offshore construction vessels, wet towing methods have been proposed to transport MBJFs, taking advantage of the buoyancy generated by suction caissons (Zhang et al., 2013; Tan et al., 2023; Fujino et al., 2023; Lian et al., 2023). Although the wet towing system can eliminate the need for large-scale barges, the lowering process of a foundation to its designated location on the seabed and the wind turbine assembly still require offshore crane vessels.

In this study, a novel construction method for MBJF wind turbines is proposed, inspired by the installation of semi-submersible wind turbines. The construction method includes wind turbine assembly on the quay, offshore wet towing, lowering operation, and penetration. The

* Corresponding author.
E-mail addresses: zhuhongzhong@riam.kyushu-u.ac.jp (H. Zhu), hu@riam.kyushu-u.ac.jp (C. Hu), swatanabe@riam.kyushu-u.ac.jp (S. Watanabe), sueyoshi@fregata.tech (M. Sueyoshi), yamashita.rikizo@obayashi.co.jp (R. Yamashita), matsuoka.yoshihiro@obayashi.co.jp (Y. Matsuoka).

https://doi.org/10.1016/j.oceaneng.2025.121740
Received 5 March 2025; Received in revised form 13 May 2025; Accepted 1 June 2025
Available online 13 June 2025
0029-8018/© 2025 The Authors. Published by Elsevier Ltd. This is an open access article under the CC BY-NC license (http://creativecommons.org/licenses/by-nc/4.0/).

Nomenclature

Symbol	
$\boldsymbol{A}$, $\boldsymbol{B}$	added mass and potential damping matrices
A_{fc}, A_{lc}	frontal and lateral projected areas
C_A	hydrodynamic coriolis-centripetal matrix
C_D	drag coefficient
C_L	lift coefficient
D_l	linear damping coefficient
D_q	nonlinear (quadratic) damping coefficient
F_e, L_e	external force and lever arm distance from the point of force application to body center
F_p	pneumatic force caused by perturbation pressure
F_t, L_t	towing force and lever arm distance from the towing point to body center
H_s	significant wave height
I_u	turbulence intensity
I_z	moment of inertia (in yaw) of the towed body
$\boldsymbol{J}$	coordinate frame transformation matrix
$K(t)$	impulse response function
L	length overall of the towed body
M_{RB}	rigid-body inertial matrix
$S(\omega)$	wave spectrum
T_z	zero-crossing wave period
U	towing speed
$U_\infty(z_h)$	mean wind speed at height z_h
V_{rel}	relative wind speed
V_r	mean speed of the towed body relative to ocean current
X, Y, and M	external loads in maneuvering model
α	towing rope angle
$\beta = \beta_w - \psi$	angle between body heading and the direction of the wave
β_w	wave propagation direction
$\boldsymbol{g}(\boldsymbol{\eta})$	restoring force
$\boldsymbol{\eta}$	position and orientation vector
$\boldsymbol{N}_n$	nonlinear damping force in maneuvering model
$\boldsymbol{\tau}_{\mathrm{external}}$	external forces and moments
$\boldsymbol{\tau}_{exc}$	wave excitation loads
$\boldsymbol{v}$	towed body velocity
$\boldsymbol{v}_r$	relative velocity w.r.t the ocean current
$\boldsymbol{V}_c$	ocean current velocity
$\boldsymbol{V}_p$	towed body horizontal velocity
γ	heat capacity ratio of air
κ	wave number
λ	scaling factor
λ_w	wave length
ℓ	spanwise length of blade element
m	mass of the towed body
m_c, V	mass and volume of the air in caisson
p, ρ	perturbation pressure and air density in caisson
p_0, ρ_0	pressure and air density at equilibrium state
q	volume changing rate of caisson
z	motion of the bucket in heave
h	displaced motion of pressure surface
ω	wave frequencies
ω_e	encounter frequency
ψ	towed body direction
ρ_a	atmospheric density
ρ_w	water density
θ	slip angle
$\lvert\Gamma\rvert$, $\angle\Gamma$	amplitude and Phase of wave exciting force RAO
$\tilde{\boldsymbol{v}}$	perturbation velocity
u_{p_r}, v_{p_r}, r_{p_r}	components of $\boldsymbol{v}_r$ associated with the body surge, sway, and yaw
u_p, v_p, r_p	components of $\boldsymbol{v}$ associated with the body surge, sway, and yaw
ϑ	angle of attack

construction process is illustrated in Fig. 1. A supplementary floater equipped with winch systems is applied to enhance the stability of the MBJF wind turbine during construction processes. As heavy offshore vessels are not required during installation and the supplementary floater is reusable, the construction duration and cost are expected to be reduced.

As the wet-towing operation encountered coupled aero-hydro loads under complicated met-ocean conditions, a feasibility study of the system considering the dynamic response, structural loads, and tugboat capability is required. To address the issues, an experimental and numerical investigation of the wet-towing system are studied in this paper. Firstly, the prototype and its scaled experimental model are developed, and experiments are conducted to study the hydrodynamics and the system behavior. Then, a numerical model that takes into account the air compressibility in suction caissons is established to describe the towing system in the seaways for dynamic analysis. The experimental results are applied to identify the damping coefficients and verify the effectiveness of the numerical model. Finally, numerical examples are conducted considering varying environmental conditions to investigate the dynamics of the wet towing system.

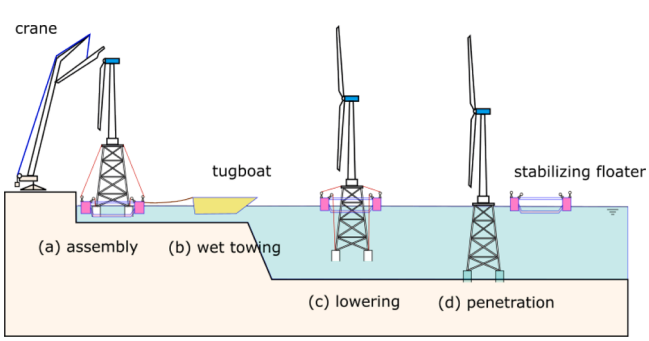

Fig. 1. Proposed construction method for MBJF wind turbine.

The remainder of this paper is organized as follows. The prototype of the towing system along with the experimental model are introduced in Section 2. Then, a numerical model considering the air compressibility in suction caissons is proposed in Section 3. After that, the experimental and numerical results are compared, and the impacts of air compressibility are discussed in Section 4, including an analysis of a circular towing operation to investigate system behavior under different ocean conditions.

2. Prototype and experimental model

The ship towing system is shown in Fig. 2. The towed body consists of a MBJF with three buckets, a 15-MW offshore wind turbine atop the MBJF, and a supplementary floater rigidly connected to the MBJF. The supplementary floater features a V-shaped geometry, facilitating straightforward mounting of the MBJF from its hollowed side. The properties of the towing system are given in Table 1. The suction caissons are partly filled with compressed air and the difference in water level inside and outside the buckets is about 10 m in still water. It should be noted that the buoyancy generated by the suction caissons is roughly equivalent to the weight of the MBJF wind turbine. In the towing operation,

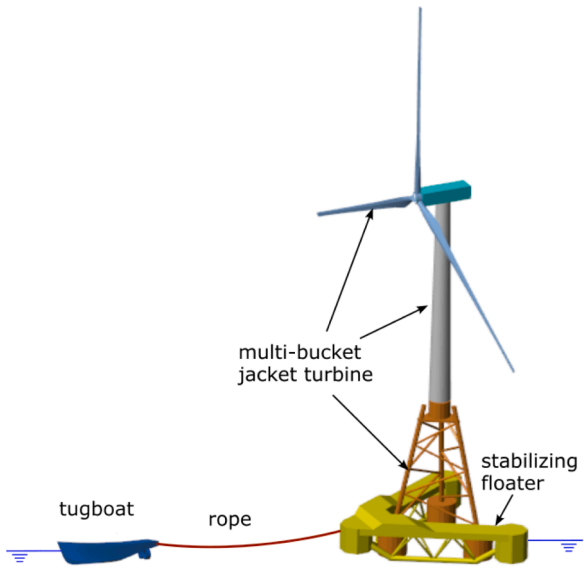

Fig. 2. Wet towing system for MBJF wind turbine with a stabilizing floater.

Table 1
Properties of FOWT.

Property	Prototype	Experimental model
Hub height	200.0 m	–
Wind turbine mass	1633 ton	–
Wind turbine CoM (w.r.t SWL)	166.7 m	–
Jacket and bucket mass	2700 ton	–
Jacket and bucket CoM (w.r.t SWL)	22.6 m	–
Jacket and bucket CoB (w.r.t SWL)	−5.1 m	−76 mm
Draft below SWL	13.0 m	193 mm
Bucket height	18.0 m	267 mm
Bucket diameter	13.5 m	200 mm
Bucket free surface elevation (w.r.t SWL)	−10 m	−148 mm
Distance between buckets (center to center)	38.7 m	573 mm
Stabilizing floater mass	4880 ton	–
Stabilizing floater mass CoM (w.r.t SWL)	2.0 m	–
Stabilizing floater CoB (w.r.t SWL)	−5.6 m	−83 mm
Distance between Stabilizing floater columns	71 m	1,052 mm
Side length of Stabilizing floater octagonal columns	7.5 m	111 mm
Total mass	9213 ton	29.9 kg
CoB of the submerged components	−5.4 m	−79 mm
Towing rope length	200 m	2,950 mm
Towing rope stiffness	744 kN/m	167 N/m
Towing speed	2 m/s	0.25 m/s

SWL: still water level.

the towing speed is supposed to be 2 m/s, with the Froude number of the towed body being approximately 0.07.

An experimental model of the towed body is developed on a scale of $\lambda = 1/67.5$ (according to the Froude similarity law), and the overview of the experimental setup is shown in Fig. 3. To accurately replicate the interaction between the water and the platform, the submerged parts are strictly designed in terms of the scaling law, while the above-water parts are designed considering the structural strength and the center of mass. The buckets, the pontoons, and the trusses are made of acrylic material and assembled using 3D printing-produced joints. Styrofoam is used to construct the three external columns of the stabilizing floater. Aluminum extrusions and aluminum pipes are used to construct the deck, the jacket, and the tower. A weight lump is installed at the top of the vertical aluminum pipe to represent the wind turbine. The main properties of the experimental model are given in Table 1 compared to the prototype. To model the spring-like effects of the towing rope in a practical system, a wire rope with a diameter of 2.5 mm and a length of 2.9 m connected serially with a spring is used. The combined spring coefficient of the towing rope is 160 N/m. A load cell (Series Number: SSK LT6-10) is applied to measure the wire tension. In addition, an air compressor and the associated piping system are applied to provide the suction caissons with compressed air.

Experiments are conducted in the towing tank installed at the Research Institute for Applied Mechanics (RIAM) of Kyushu University, which measures 65 m in length, 5 m in width, and 7 m in depth. In the tank, a plunger-type wave generator is installed at one end, while a wave absorber is on the opposite side.A wave probe is installed 10 m in front of the wave generator, near the sidewall of the towing tank. This placement avoids the need for supporting structures in the central area, which could interfere with the towing operation. Three differential-type pressure transducers (Type: PA-100-200D-W) with a range in $-2 \sim 2$ kPa are employed for measuring the pneumatic pressure in the suction caissons. In addition, four optical cameras (Optitrack, Flex13) are installed on the towing carriage to record the motion of the towed body.

In this study, four types of experiments are conducted to investigate the system behavior and stability of the towing system: free decay tests of the towed body, course stability tests, static oblique towing tests, and towing tests in regular waves. The free decay tests and the course stability tests are performed to investigate the natural frequencies and damping characteristics of the towed body, as well as to assess the course stability performance of the towing system. The static oblique towing tests are designed to measure the current coefficients of the towed body, while the towing tests in regular waves are carried out to examine the motion response under wave loads and to validate the numerical model.

Free decay tests for the towed body in heave, roll, and pitch are conducted with the model freely floating on the water surface. The model is manually displaced from its equilibrium position, and then released, allowing it to oscillate freely in calm water. In addition, a free decay test in surge is performed during straight-line towing. In this case, the carriage maintains a constant speed while the velocity of the towed body is temporarily reduced to induce a surge disturbance. Due to the elasticity of the towing rope, the surge velocity exhibits damped oscillations. Furthermore, an experiment is designed to investigate the oscillating behavior of the water surface in a bucket. In this experiment, the caisson is open to atmosphere, and the water column height is set to 44 mm, matching the water column height of the prototype bucket when scaled. An initial disturbance is applied using a vertical disc to displace the water surface, which is then allowed to oscillate freely under gravity. The motion of the water surface is captured using a high-speed camera.

The course stability tests are conducted under straight-line towing in calm water at constant speed. An external impulse disturbance is applied laterally to the towed body to induce its sway and yaw motion, and the subsequent attenuation of these motions is used to evaluate the course stability performance of the towing system.

In the static oblique towing tests, the towed body is rigidly attached to the towing carriage and moved at constant speed in calm water. The drag force, lift force, and yaw moment are measured as functions of yaw angle using a six-component strain gauge (Serial Number: LMC-6566-200NWP-K). Moreover, towing tests in regular waves are conducted under head-wave conditions. To prevent lateral drift and ensure safety, two loosely securing ropes are bolted to the left and right sides of the platform. The wave conditions used in these tests are summarized in Table 2.

The experiments provide essential data for analyzing the behavior of the towing system, identifying the hydrodynamic coefficients, and validating the numerical model. A numerical model is proposed in Section 3 to describe the system dynamics, and a comparison between the experimental and numerical results is presented in Section 4.

3. Numerical model

Since the Froude number of the platform at a constant speed of 2 m/s is approximately 0.07, the towed body can be categorized as a *Displacement vessel*, allowing the application of potential theory to compute hy-

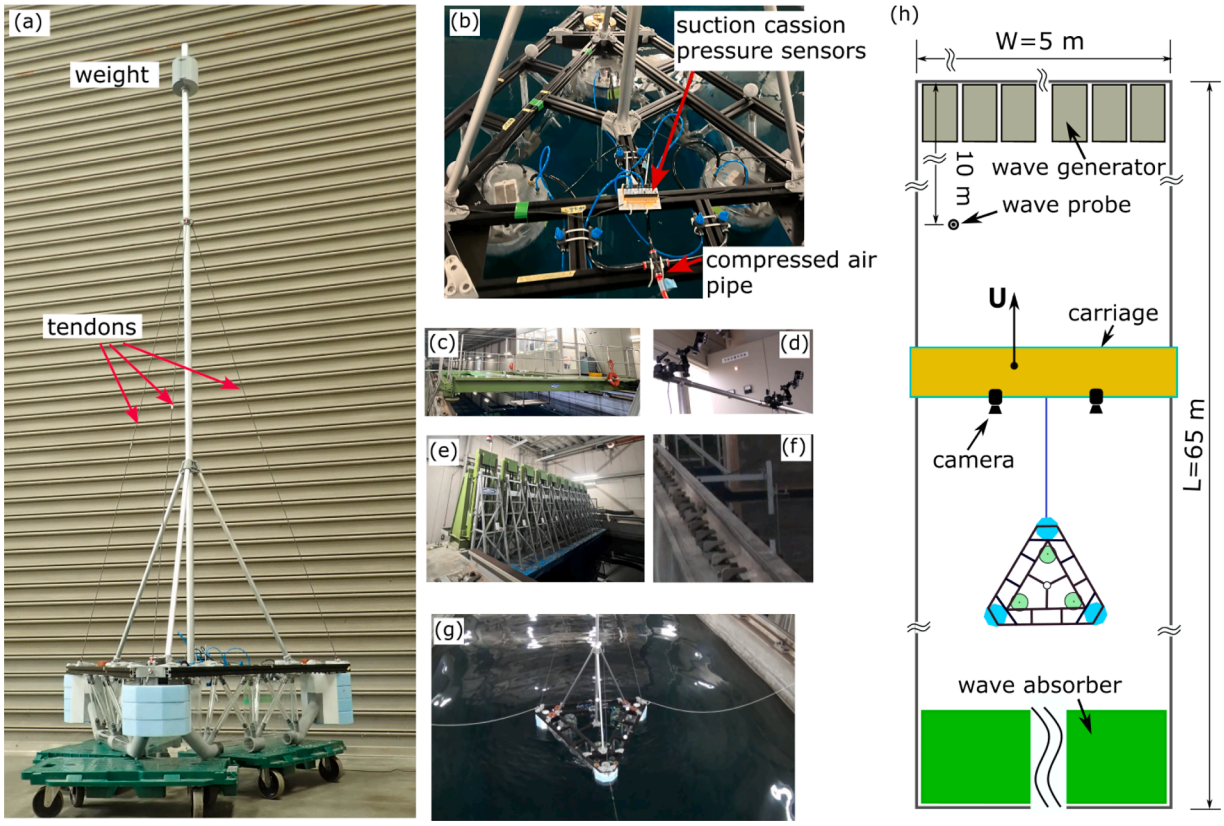

Fig. 3. Experimental model: (a) overview, (b) top view, (c) towing carriage, (d) optical cameras, (e) wave generator, (f) wave probe, (g) towing experiment scene, and (h) plan view of the towing system.

Table 2
Regular waves for experiments. The values in parentheses after '/' are the corresponded values in prototype.

Case	Wave height	Wave period
1	3 cm / (2 m)	0.70 s / (5.75 s)
2	3 cm / (2 m)	0.80 s / (6.57 s)
3	3 cm / (2 m)	1.00 s / (8.22 s)
4	3 cm / (2 m)	1.20 s / (9.86 s)
5	3 cm / (2 m)	1.40 s / (11.50 s)
6	3 cm / (2 m)	1.60 s / (13.15 s)
7	3 cm / (2 m)	1.80 s / (14.79 s)
8	3 cm / (2 m)	2.00 s / (16.43 s)

drodynamic coefficients (Fossen, 2011). The *airy wave theory* and *superposition principle* are applied to model the towing system. In addition, the following assumptions are applied:

- The MBJF, stabilizing floater, and their connection mechanism are rigid.
- The wave-making effects and the wave-current interaction are neglected.
- The ocean current is constant and irrotational.
- The hydrodynamic scaling effects are ignorable so that experimental measurements are applicable for damping estimation.

In addition, as the diameter of the bucket is small compared to practical wavelengths, only the pumping motion is considered for the pressure surfaces. For ease of studying the dynamics of the towed body, the tugboat is treated as a point mass moving with a constant speed.

For the modeling, the Global coordinate system is defined on the still water level. The XY plane coincides with the still water surface and the X-axis points from the West to the East. The Z-axis points vertically downwards, and the Y-axis is determined according to the right-hand rule. A body-fixed coordinate system, with its origin aligned at the center of the undisturbed water plane area, is applied to define the platform motion and the hydro loads. The coordinate systems are illustrated in Fig. 4(a). In the figure, the term U is the towing speed, $\boldsymbol{V}_c$ the ocean current, V_p the platform velocity, α the towing rope angle, and θ the slip angle.

3.1. Structural modeling

Simscape Multibody® (MathWorks, 2024), a simulation environment for 3D multibody mechanical systems, is used to model the structure of the towing system. In the toolbox, each component is represented by blocks that define bodies, joints, constraints, force, and sensors. The model is illustrated in Fig. 5. A six-degree-of-freedom (6-DOF) joint is applied to connect the MBJF to the Global coordinate frame. The stabilizing floater, tower, nacelle, and rotor are sequentially connected through appropriate coordinate transformation blocks to establish the complete structural assembly. A linear spring block is implemented to model the towing rope that connects the towed body and the tugboat. User-defined function blocks are employed to compute aerodynamic and hydrodynamic loads based on time series met-ocean data and the instantaneous motion of the body. These forces are applied to the model using external force blocks. It should be noted that, at this stage of the study, the flexibility of the blades and the tower is not considered.

For the towed body, the motion can be expressed by Fossen (2011)

$$\dot{\boldsymbol{\eta}} = \boldsymbol{J}(\eta)\boldsymbol{\nu}, \tag{1}$$

$$\boldsymbol{M}_{RB}\dot{\boldsymbol{\nu}} + \boldsymbol{C}_{RB}(\boldsymbol{\nu})\boldsymbol{\nu} = \boldsymbol{\tau}_{\text{external}}, \tag{2}$$

where $\boldsymbol{\nu} \in \mathbb{R}^6$ is the velocity vector expressed in the body-fixed coordinate frame, $\boldsymbol{\eta} \in \mathbb{R}^3 \times \mathbb{S}^3$ the position and orientation vector expressed in Global coordinate frame, $\boldsymbol{J}$ the frame transformation matrix, $\boldsymbol{M}_{RB}$ the rigid-body inertia matrix, $\boldsymbol{C}_{RB}$ the rigid-body Coriolis-Centripetal matrix

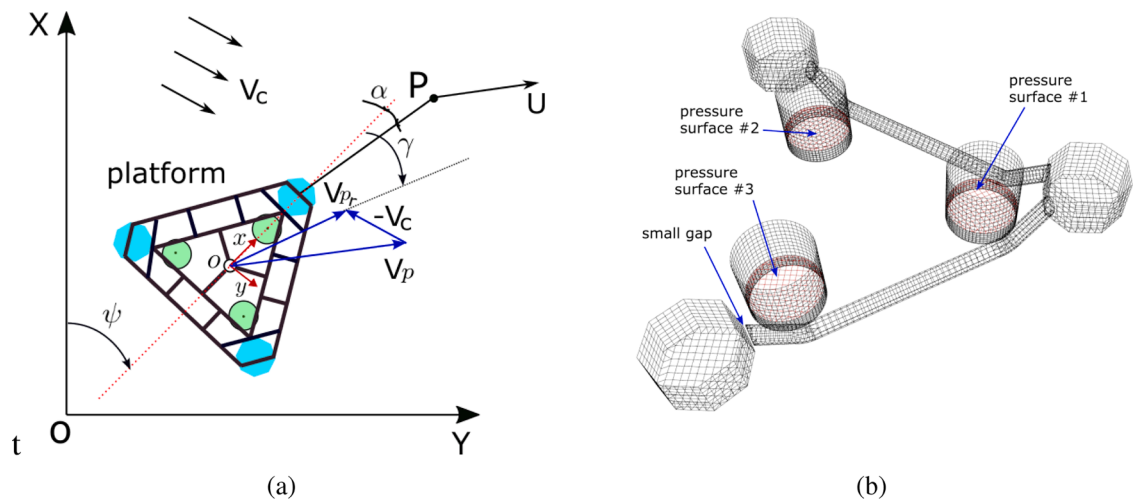

Fig. 4. Towing system: (a) coordinate system; (b) panel mesh in WAMIT (7173 panels for the wet surface; 185 panels for each pressure surface.

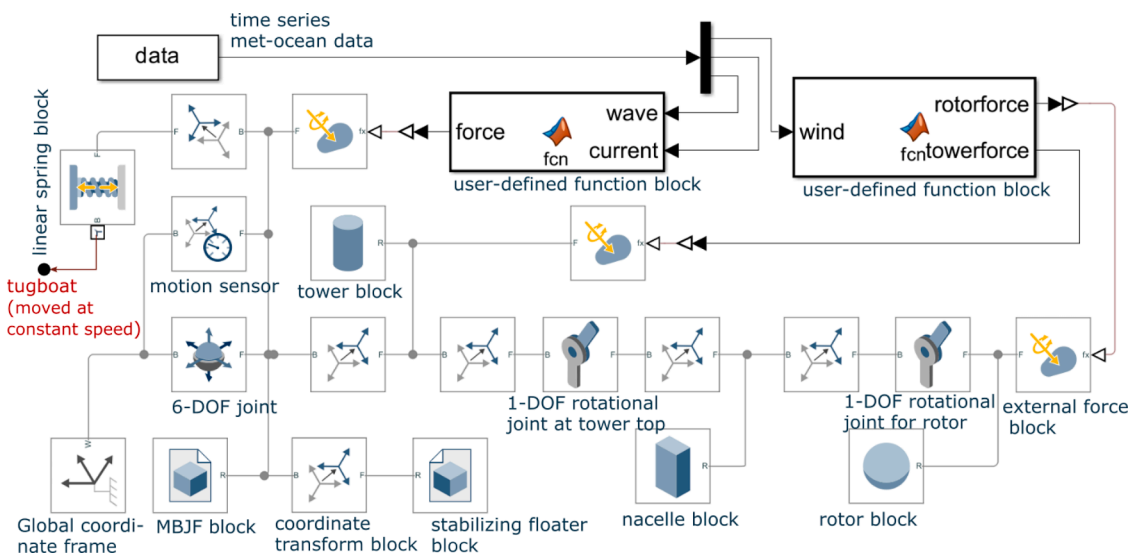

Fig. 5. Numerical model of the towed body in Simulink.

due to the rotation, and $\boldsymbol{\tau}_{\text{external}}$ the external forces and moments due to the gravitational and buoyancy forces, aero- and hydro-dynamics, and the towing force from the towing rope. In Simulink^{TM}, the kinematic Eq. (1) and the kinetic Eq. (2) can be solved automatically when external forces are provided. In the following Sections 3.2 and 3.3, the external loads applied to the towed body are explained.

3.2. Aerodynamics

In the towing process, the wind turbine is in a shutdown state with the blades feathered. The aerodynamic forces acting on the wind turbine are calculated by integrating the distributed loads along the span of each blade and the height of the tower. These loads are evaluated using blade element theory, where the local wind conditions, blade geometry, and motion are considered for each discrete element. Defining C_L and C_D as the lift and drag coefficients, the forces on each discrete element are expressed by

$$f_L = \frac{1}{2}\rho_a c V_{\text{rel}}^2 C_L(\vartheta)\ell, \tag{3}$$

$$f_D = \frac{1}{2}\rho_a c V_{\text{rel}}^2 C_D(\vartheta)\ell, \tag{4}$$

where ρ_a is the air density, c the chord length, V_{rel} the relative wind speed, ϑ the angle of attack, and ℓ the span-wise length of the element. Blade information, including the lift and drag coefficients, is obtained from the IEA 15-MW offshore reference turbine (Gaertner et al., 2020).

3.3. Hydrodynamics

The hydro loads on the platform are composed of maneuvering resistance, seakeeping, damping, restoring, and wave excitation terms. Based on the unified seakeeping and maneuvering theory (Fossen, 2011), the hydrodynamic loads can be expressed by:

$$\begin{aligned}\boldsymbol{\tau}_{hd} = &-\underbrace{\left(\boldsymbol{A}(0)\dot{\boldsymbol{v}}_r + \boldsymbol{C}_A(\boldsymbol{v}_r)\boldsymbol{v}_r + \boldsymbol{N}_n(\theta, V_r)\right)}_{\text{maneuvering resistance}} \\ &-\underbrace{\left(\boldsymbol{A}(\infty)\dot{\tilde{\boldsymbol{v}}} + \int_0^t \boldsymbol{K}(t-\tau)\tilde{\boldsymbol{v}}(\tau)d\tau\right)}_{\text{seakeeping terms}} - \underbrace{\left(\boldsymbol{D}_l\tilde{\boldsymbol{v}} + \boldsymbol{D}_q\tilde{\boldsymbol{v}}|\tilde{\boldsymbol{v}}|\right)}_{\text{damping terms}} - \underbrace{\boldsymbol{g}(\boldsymbol{\eta})}_{\text{restoring term}} \\ &+ \underbrace{\boldsymbol{\tau}_{exc}}_{\text{wave excitation term}},\end{aligned} \tag{5}$$

where $\boldsymbol{v}_r = \boldsymbol{v} - \boldsymbol{V}_c$ is the relative velocity with respect to the ocean current, V_r the mean relative horizontal speed, $\tilde{\boldsymbol{v}}$ the perturbation velocity, $\boldsymbol{A}(0)$ and $\boldsymbol{A}(\infty)$ the zero-frequency and infinite-frequency added mass

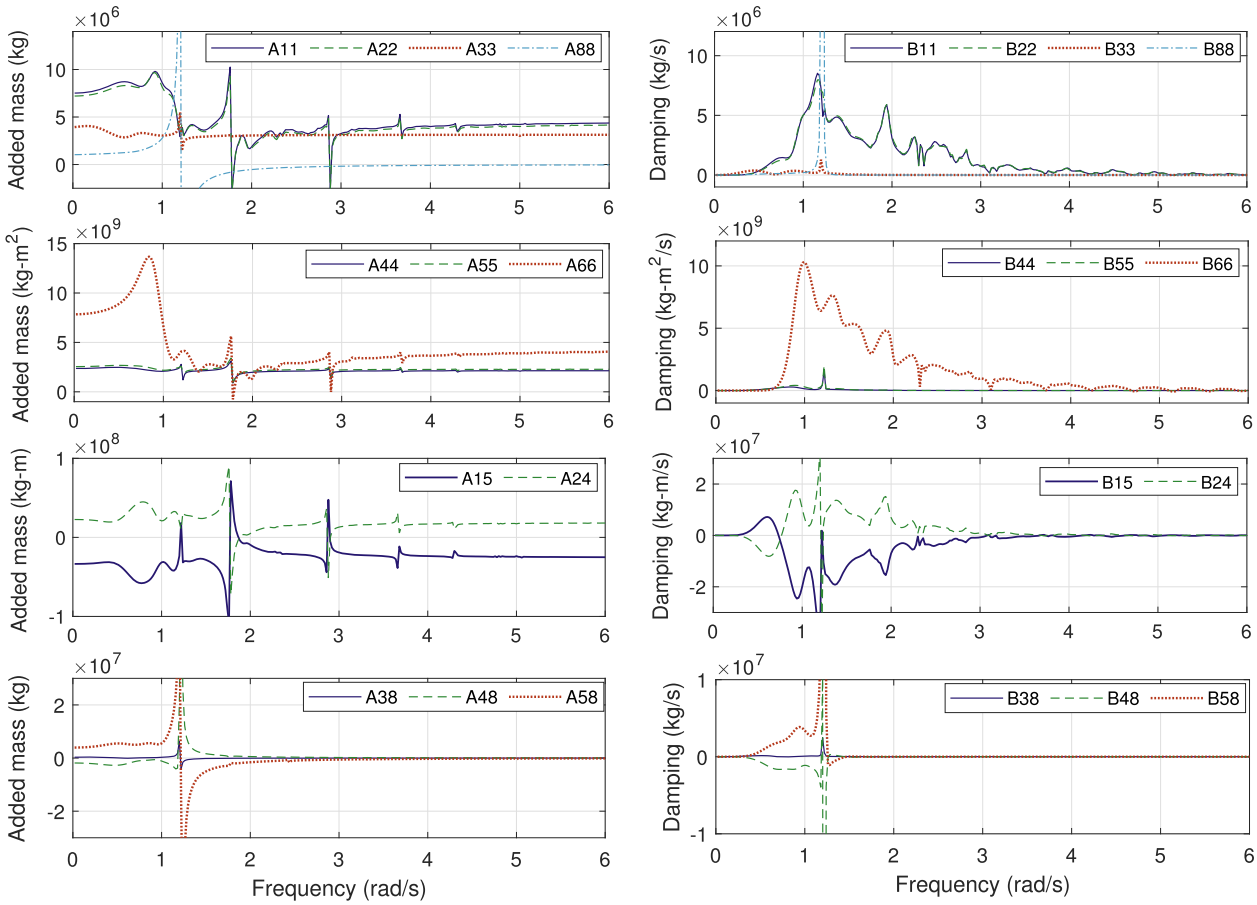

Fig. 6. Added mass (left) and radiation damping (right).

matrices, respectively, C_A the hydrodynamic Coriolis-Centripetal matrix, $\boldsymbol{N}_n(\gamma, V_r)$ the nonlinear damping force to account for the steady-state nonlinear surge damping and the cross-flow drag on the hull in the maneuvering model, $K(t)$ the impulse response function (or retardation function), D_l and D_q the linear and nonlinear damping coefficients, $\boldsymbol{g}(\boldsymbol{\eta})$ the restoring force, and $\boldsymbol{\tau}_{exc}$ the wave excitation loads. The maneuvering resistance terms consider the low-frequency loads in surge, sway, and yaw, which will be detailed in Section 3.3.3.

The linear diffraction-radiation software WAMIT (Version 7.4) (Lee and Newman, 2016) is applied to compute the first-order hydrodynamic coefficients, including added mass, potential damping, hydrostatic restoring coefficients, and wave excitation forces. The panel model used in the computations consists of a structural mesh and three pressure-surface meshes, as illustrated in Fig. 4(b). The computation involves 9 DOFs: 6 DOFs correspond to the motion of the towed body, while the remaining three represent the pumping motions of the pressure surfaces. The WAMIT subroutine 'NEWMODES' is modified to incorporate these additional pressure surface modes.

To simplify the panel model, small gaps are introduced between the vertical columns and the lower pontoons, and the mesh for the truss structure—used for structural reinforcement—is omitted. The computed added mass and radiation damping coefficients are shown in Fig. 6 as functions of the platform response frequencies. Due to the geometric symmetry of the platform and the identical configuration of the pressure surfaces, only the diagonal terms and the upper off-diagonal terms related to the towed body and the second pressure surface are plotted. The Response Amplitude Operators (RAOs) for the first-order wave excitation force are provided in Fig. 7 for wave headings of 0°, 30°, and 60°. In the figures, the subscript $_{ij}$ represents the property (added mass or retardation function) of the ith DOF due to the motion in the jth DOF. Here, $i, j = 1, 2 \ldots, 6$ correspond to the platform motions, while $i, j = 7, 8, 9$ correspond to the pressure surfaces. Sharp changes observed in the coefficients associated with heave motion of the platform and pressure surfaces ($i, j = 3$ and $i, j = 7, 8, 9$) near 1.22 rad/s are attributed to the pumping modes of the pressure surfaces. In addition, peaks near 1.76 rad/s and 2.88 rad/s are considered to result from sloshing modes within the suction buckets. It is also noted that negative added mass values occur due to free-surface effects.

3.3.1. Impulse response functions

Based on the potential damping coefficients computed by WAMIT, the retardation function K in (5) can be calculated by

$$K_{ij}(t) = \frac{2}{\pi}\int_0^{\infty} \boldsymbol{B}_{ij}(\omega)\cos(\omega t)d\omega, \quad i, j = 1, 2 \ldots, 9 \tag{6}$$

Since viscous damping is not captured in potential-flow theory, the impulse response functions associated with the pressure surfaces—calculated by (6)—exhibit undamped or weakly damped oscillations that persist over an extended duration, as illustrated by the solid line in Fig. 8. This prolonged response imposes a significant computational burden during convolution operations in (5). To mitigate this issue, a post-processing program is developed to introduce a constant linear damping ratio of 7 % across all frequencies to improve the damping, and the result is compared in Fig. 8. The choice of 7 % is based on the comparative study of numerical and experimental results for an oscillating water column in Aubault et al. (2011).

3.3.2. Wave excitation forces

Suppose that the towing operation is carried out in long-crested seas, the wave excitation force $\boldsymbol{\tau}_{exc}$ can then be computed based on force

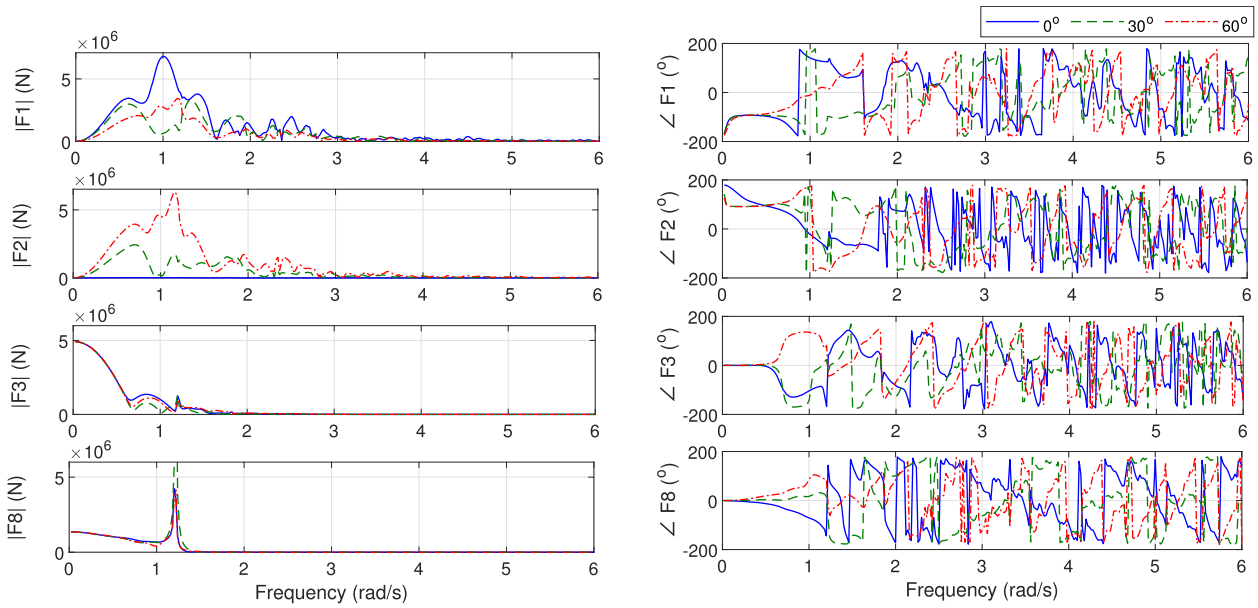

(a) Wave excitation force RAOs for translational DOFs.

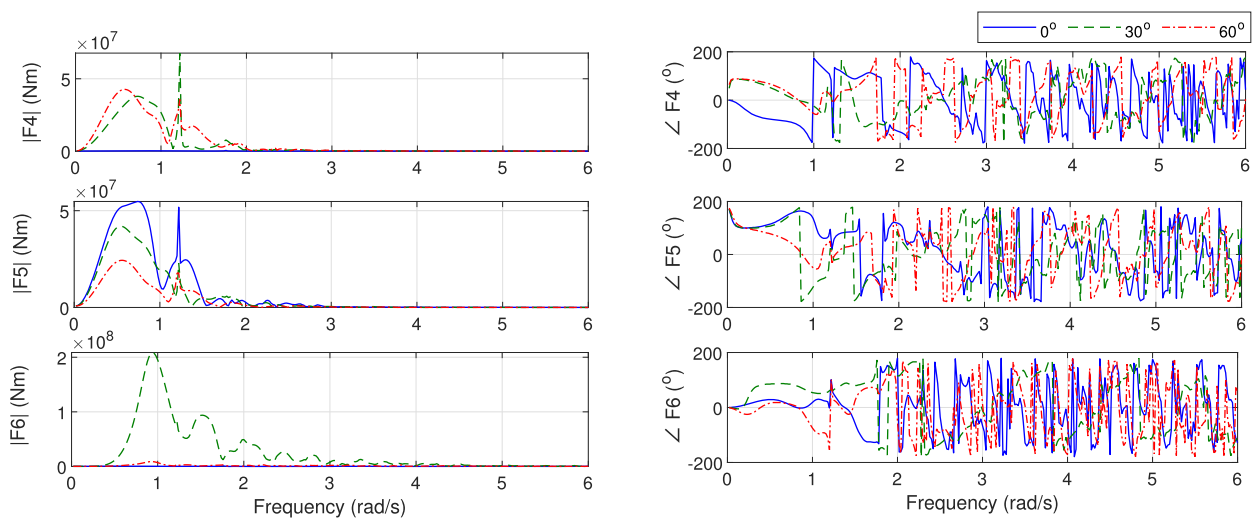

(b) Wave excitation force RAOs for rotational DOFs.

Fig. 7. First-order wave excitation force RAOs. The left graphs show the force amplitudes and the right graphs show the corresponding phases.

RAOs by

$$\boldsymbol{\tau}_{exc} = \sum_{j=1}^{N} |\Gamma(\omega_{e_j}, \beta)| \sqrt{2S(\omega_j)\Delta\omega} \cdot \cos\left(\omega_j t - \kappa_j(x\cos\beta_w + y\sin\beta_w) + \angle\Gamma(\omega_{e_j}, \beta) + \epsilon_j\right), \tag{7}$$

where $|\Gamma|$ and $\angle\Gamma$ are the amplitude and phase of the force RAO, respectively, $S(\omega)$ the wave spectrum, ω the wave frequency, ω_e the encounter frequency, β_w the wave propagation direction, $\beta = \beta_w - \psi$ the angle between the heading and the direction of the wave, κ the wave number, ϵ the random phase angles, and $\Delta\omega$ the constant difference between the successive frequencies.

3.3.3. Maneuvering coefficients

The maneuvering model in (5) accounts for the low-frequency horizontal motion (surge, sway, and yaw). The associated hydrodynamic coefficients are expressed by Fossen (2011):

$$A(0)^{1,2,6} = \begin{bmatrix} A_{11}(0) & 0 & 0 \\ 0 & A_{22}(0) & A_{26}(0) \\ 0 & A_{62}(0) & A_{66}(0) \end{bmatrix}, \quad (A_{26}(0) = A_{62}(0)), \tag{8}$$

$$C_A^{1,2,6}(\boldsymbol{v}_r) = \begin{bmatrix} 0 & 0 & -A_{22}(0)v_{p_r} - A_{26}(0)r_{p_r} \\ 0 & 0 & A_{11}(0)u_{p_r} \\ A_{22}(0)v_{p_r} + A_{26}(0)r_{p_r} & -A_{11}(0)u_{p_r} & 0 \end{bmatrix}, \tag{9}$$

where u_{p_r}, v_{p_r}, and r_{p_r} are the components of $\boldsymbol{v}_r$ associated with the platform surge, sway, and yaw, respectively. In addition, the nonlinear damping $\boldsymbol{N}_n(\gamma, V_r)$ to consider the surge drag, the cross-flow force, and the moment on the hull are calculated using the current coefficients:

$$\boldsymbol{N}_n^{1,2,6} = \begin{bmatrix} \frac{1}{2}\rho_w A_{\mathrm{fc}} C_x(\theta) V_r^2 \\ \frac{1}{2}\rho_w A_{\mathrm{lc}} C_y(\theta) V_r^2 \\ \frac{1}{2}\rho_w A_{\mathrm{lc}} L C_n(\theta) V_r^2 \end{bmatrix}. \tag{10}$$

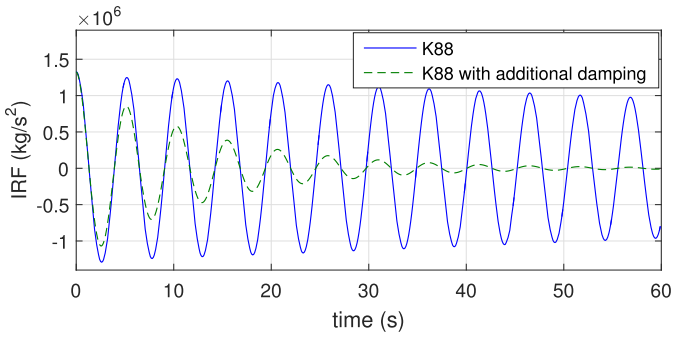

Fig. 8. Impulse response function of the second pressure surface.

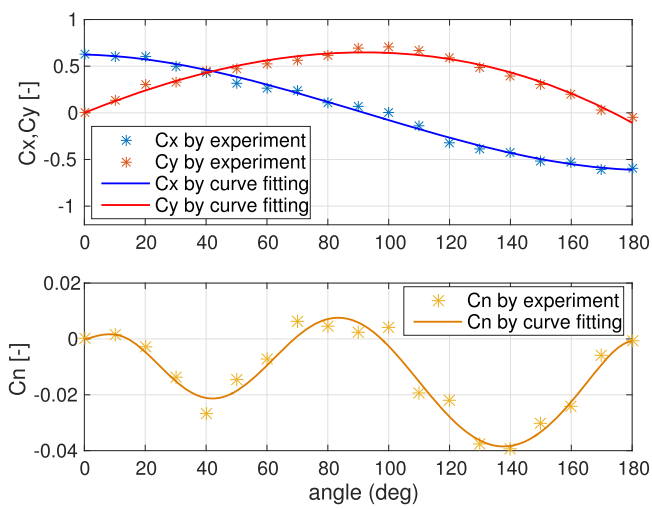

Fig. 9. Current coefficients.

where A_{fc} and A_{lc} are the frontal and lateral projected areas, respectively, L is the length overall of the towed body on the still water surface. The current coefficients are derived based on experimental results, as illustrated in Fig. 9. A curve fitting approach is applied to reconstruct the coefficients, ensuring that they vary continuously as functions of the angle of slip θ.

3.4. Thermodynamics in suction caissons

The pneumatic pressure in the suction caissons can be obtained by analyzing the thermodynamic process. If the air in the caissons is assumed to be ideal and the air compression and decompression are isentropic processes, the air density as a function of pressure can be expressed by:

$$\frac{\rho}{\rho_0} = \left(\frac{p_0 + p}{p_0}\right)^{1/\gamma_0}, \tag{11}$$

where ρ is the air density in the caisson, p the perturbation pressure, ρ_0 and p_0 the air density and pressure at the equilibrium state, respectively, and $\gamma_0 = 1.4$ the heat capacity ratio of air. Due to the mass conservation, the air density variation can be written as

$$\frac{dm_c}{dt} = V\frac{d\rho}{dt} - \rho q = 0, \tag{12}$$

where m_c and V are the mass and volume of the air in the caisson, respectively, q is the volume changing rate of the caisson. Based on (11) and (12), the pressure perturbation can be expressed by

$$\frac{V}{\gamma_0(p_0 + p)}\frac{dp}{dt} - A_c(\dot{h} - \dot{z}) = 0 \tag{13}$$

where h is the displaced motion of the pressure surface, z is the motion of the bucket in heave, and A_c is the cross-sectional area of the caisson.

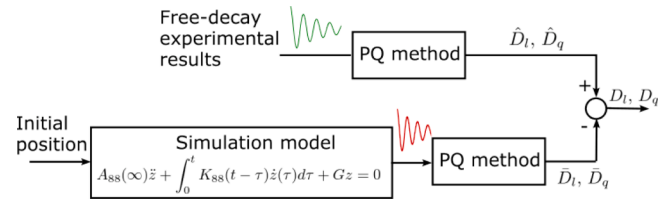

Fig. 10. Approach to determine damping coefficients.

Based on the perturbed pressure p, the pneumatic load on the associated bucket and pressure surface becomes $F_p = pA_c$.

3.5. Identification of damping coefficients

In this section, the experimental results are utilized to identify the damping coefficients D_l and D_q in(5). Before the identification, the following settings in the numerical model are modified to reflect the experiment-specific properties:

- A point mass is applied to represent the wind turbine.
- The structural mass is reduced by a factor of 1/1.025 to account for the difference in water density between freshwater and seawater.

To enable the use of experimental results for identifying damping coefficients, both thermodynamic similarity and Froude similarity between the experimental model and the prototype must be satisfied. To this end, the heat capacity in the numerical model is adjusted accordingly. Further details are provided in the following subsection.

3.5.1. Scale effects of suction caissons

From (12), the following equation needs to be satisfied to maintain the thermodynamics similarity (Falcão and Henriques, 2019):

$$\left(\frac{V}{\gamma_0(p_0 + p)q}\frac{dp}{dt}\right)_{\text{pt}} = \left(\frac{V}{\gamma_0(p_0 + p)q}\frac{dp}{dt}\right)_{\text{exmdl}}. \tag{14}$$

The subscripts 'pt' and 'exmdl' stand for prototype and experimental model, respectively. Froude similarity law requires that

$$\frac{V_{\text{exmdl}}}{V_{\text{pt}}} = \lambda^3, \qquad \frac{q_{\text{exmdl}}}{q_{\text{pt}}} = \lambda^{2.5}, \tag{15}$$

$$\frac{(\gamma_0(p_0 + p))_{\text{exmdl}}}{(\gamma_0(p_0 + p))_{\text{pt}}} = \delta\lambda, \qquad \frac{(dp/dt)_{\text{exmdl}}}{(dp/dt)_{\text{pt}}} = \delta\lambda^{1/2}, \tag{16}$$

where $\delta = (\rho_{w_{\text{exmdl}}}/\rho_{w_{\text{pt}}})$ denotes the ratio of water density between freshwater in the model test and seawater in the prototype. The conditions in (15) are inherently satisfied, as they have been considered in the experimental model design. However, the conditions in (16) are not met since the ambient pressure in both the experimental and full-scale systems corresponds to atmospheric pressure (i.e., $\gamma_{\text{exmdl}} = \gamma_{\text{pt}}$) and the pressure in caissons satisfies $\frac{(p_0)_{\text{exmdl}}}{(p_0)_{\text{pt}}} \approx \frac{1}{2}$. To ensure both thermodynamics similarity (14) and Froude similarity, the heat capacity γ_0 in (14) is adjusted as:

$$\begin{aligned}\gamma_{0_{\text{pt}}} &= \frac{1}{\delta\lambda}\frac{(p_0 + p)_{\text{exmdl}}}{(p_0 + p)_{\text{pt}}}\gamma_{0_{\text{exmdl}}}, \\ &\approx \frac{1}{2\delta\lambda}\gamma_0,\end{aligned} \tag{17}$$

where the perturbed pressure p is neglected, as its magnitude is relatively small compared to p_0.

3.5.2. Damping estimation

The damping coefficients are estimated based on the results of free decay tests, starting with the evaluation of damping for the pressure surfaces. Since the caisson is open to atmosphere during testing, as explained in Section 2, the thermodynamic model is not required for

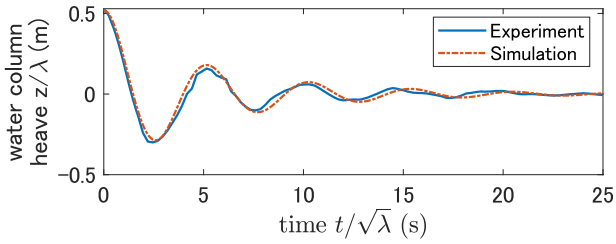

Fig. 11. Free decay results of water column.

the estimation. The identification approach is based on the PQ method (Wang et al., 2022; Mauro and Nabergoj, 2021), as shown in Fig. 10. Total damping is first extracted from the free decay response, and the linear and nonlinear damping components are then determined by subtracting the potential damping, computed from numerical simulations, from the total damping. The *Cummins Equation* is used to model the water surface motion in the time domain. Once estimated, the linear and nonlinear damping terms are incorporated into the *Cummins Equation* to enhance modeling accuracy. A comparison between experimental and numerical results is presented in Fig. 11, showing good agreement and validating the effectiveness of the proposed estimation approach.

The same approach is applied to estimate the damping coefficients in surge, heave, and pitch. The simulation results incorporating the estimated damping terms are compared with experimental data in Fig. 12. The close agreement between the results confirms the validity and effectiveness of the damping estimation method.

The damping coefficients in sway and yaw for the platform are estimated based on the course stability tests. The following maneuvering model (Yasukawa and Yoshimura, 2015) is applied to describe the motion of the towed body in the tests:

$$\left(m + A_{11}(0)\right)\dot{u}_p - \left(m + A_{22}(0)\right)v_p r_p + \boldsymbol{N}_n^1 = X, \tag{18}$$

$$\left(m + A_{22}(0)\right)\dot{v}_p + \left(m + A_{11}(0)\right)u_p r_p + \boldsymbol{N}_n^2 = Y, \tag{19}$$

$$\left(I_z + A_{66}(0)\right)\dot{r}_p + \boldsymbol{N}_n^6 = M, \tag{20}$$

where m and I_z are respectively the mass and the moment of inertial of the platform, $\boldsymbol{N}_n^i$ $(i = 1, 2, 6)$ is the $i - th$ components of $\boldsymbol{N}_n$ in (10). The terms X, Y, and M are the external forces, including the damping terms to be estimated, the towing force, and the external force to disturb the straight-line motion:

$$X = -D_{l_{11}}u_p - D_{q_{11}}|u_p|u_p + F_t\cos\alpha, \tag{21}$$

$$Y = -D_{l_{22}}v_p - D_{q_{22}}|v_p|v_p + F_t\sin\alpha + F_e, \tag{22}$$

$$M = -D_{l_{66}}r_p - D_{q_{66}}|r_p|r_p + F_t L_t\sin\alpha + F_e L_e, \tag{23}$$

where $D_{l_{jj}}$ and $D_{q_{jj}}$ are the jj-element of D_l and D_q, F_t the towing force, L_t the distance from the towing point on the platform to the platform center, F_e the external force applied during the tests, and L_e the lever arm distance from the point of force application to the platform center. The cross-coupling resistance terms involving v_p and r_p are neglected in this analysis.

Since the time series data of the towing and external force are measured in the experiments, the damping coefficients can be estimated using a least-square approach (Chan et al., 1995). The numerical results using the estimated damping coefficients are shown as dot-dashed lines in Fig. 13, in comparison with the experimental results. As the sway-roll coupling effects—responsible for the high-frequency sway motion observed in the experimental results—are not accounted for in the maneuvering model (18)~(20), these high-frequency components are not fully reproduced. However, as such components are not the focus of the maneuvering model, they are not intended to be captured. Therefore, it can be concluded that the numerical model successfully represents the dominant dynamics, including the course stability behavior and overall oscillation patterns.

4. Results and discussion

The numerical model established in Section 3 is applied in this section to study the system dynamics, including the influence of air compressibility in the suction caissons on the motion of the towed body. The thermodynamic model is studied under two configurations: one with $\gamma = \gamma_0/(2\delta\lambda)$, representing the experimental condition with low air

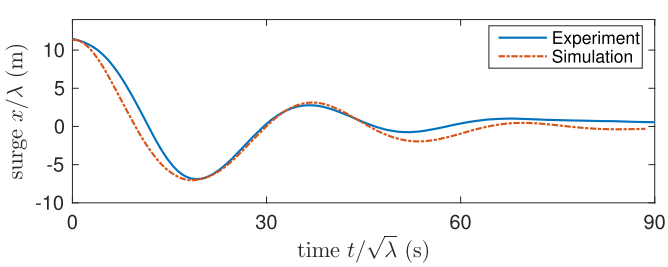

(a) Free decay results in surge.

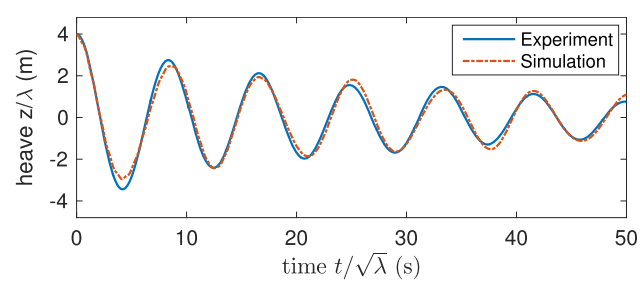

(b) Free decay results in heave.

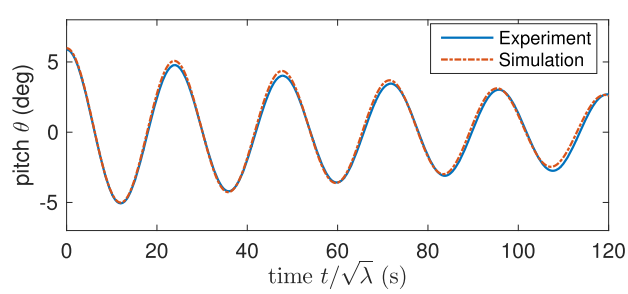

(c) Free decay results in pitch.

Fig. 12. Free decay test results in surge, heave, and pitch. The surge tests are conducted during the towing operations, while the heave and pitch tests are performed in calm water with the platform freely floating in calm water.

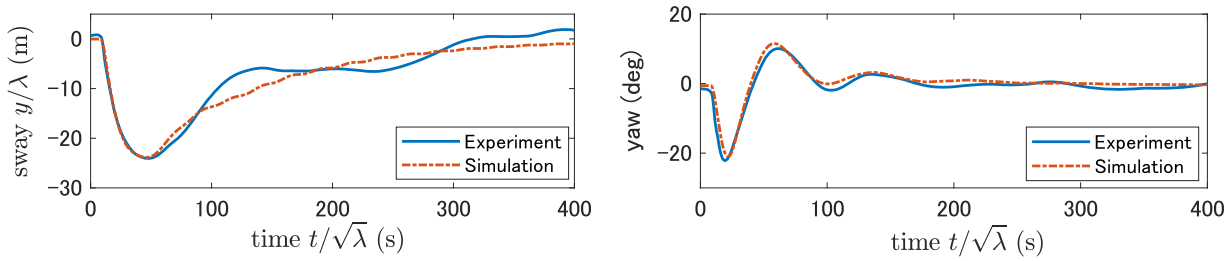

Fig. 13. Comparison of the response of sway (left graph) and yaw (right graph) after a perturbation from the side of the platform.

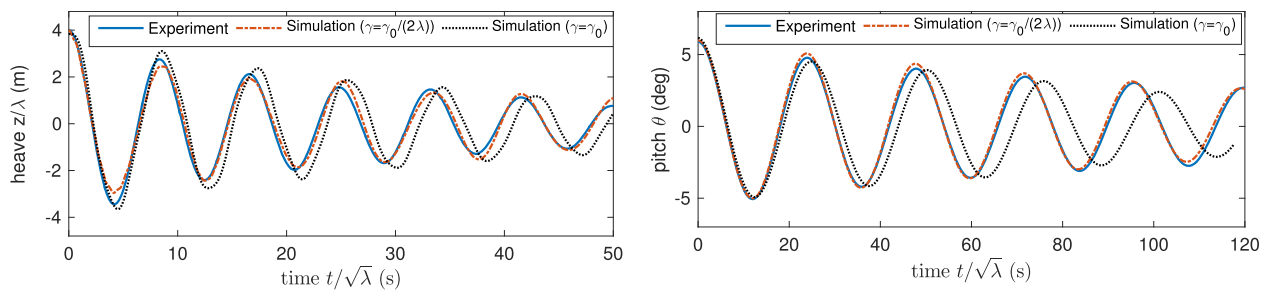

(a) Free decay results in heave. (b) Free decay results in pitch.

Fig. 14. Comparison of the free decay results in heave and pitch. The cases with $\gamma = \gamma_0$ record larger oscillating periods due to reduced restoring performance. It is worth noting that the damping effects in heave are reduced, while those in pitch are increased.

Table 3
Comparison of motion characteristics under low air compressibility (experimental condition) and realistic air compressibility (practical condition).

Motion property	Low air compressibility $\gamma = \gamma_0/(2\delta\lambda)$	Realistic situation $\gamma = \gamma_0$	Variation
Heave natural period	8.3 s	8.6 s	3.5 %
Heave damping factor	5.7 %	4.2 %	−16 %
Pitch natural period	23.8 s	24.9 s	3.8 %
Pitch damping factor	2.8 %	3.5 %	25 %

compressibility, and another with $\gamma = \gamma_0$, reflecting prototype condition. These models are used to analyze the free-decay response and the response under regular waves, in comparison with experimental results. Finally, a towing operation involving circular motion under combined wind, wave, and current conditions is examined to investigate the system response under realistic met-ocean conditions.

4.1. Free decay tests

Since air compressibility in the suction caissons primarily affects the vertical motion of the towed body, free decay tests in heave and pitch are analyzed using the two previously explained configurations. The corresponding results are shown in Fig. 14, alongside the experimental results. The results indicate that the natural frequencies in both heave and pitch decrease under the configuration $\gamma = \gamma_0$, due to the reduced restoring stiffness. In addition, a reduction in heave damping and an enhancement in pitch damping are observed. These motion characteristics are summarized in Table 3. The behavior can be attributed to the proximity of the heave natural frequency to the pumping mode frequency of the pressure surfaces, which leads to a reduced damping effect due to resonance. In contrast, the pitch natural frequency lies outside the resonant region, allowing the damping pool effect (Ikoma et al., 2021; Chuang et al., 2021) to contribute more effectively to energy dissipation.

4.2. Towing responses under regular waves

While free decay tests provide valuable insight into the natural frequencies and damping characteristics, they only reflect the system's response under initial conditions. To comprehensively validate the numerical model and assess its predictive performance under realistic sea conditions, it is essential to examine the responses of the towing system under waves.

In the numerical simulations, the wave height is set to 2.0 m, and the wave periods range from 5.5 s to 20 s in 0.8 s intervals, covering the conditions as those used in the experiments. Each simulation runs for 600 s, with the first 100 s considered as the transient process and excluded from the analysis. The RAOs of the platform motion, the pressures in the suction caissons, and the towing force are evaluated, as shown in Fig. 15. The results show that the platform motion RAOs are small in short waves and tend to increase in long waves. For heave, the RAO increases gradually as the wave frequency approaches its natural frequency, and asymptotically approaches 1 in long waves. In contrast, for surge and pitch, whose natural frequencies lie below the range of the simulated wave frequencies, the RAOs increase continuously with wave period. In addition, the towing force response closely follows that of surge motion, which is expected since the waves are aligned head-on with the towing direction. It is also observed that the numerical model with $\gamma = \gamma_0/(2\delta\lambda)$ provides a better match with the experimental results, as it accounts for the low air compressibility in the suction caissons—consistent with the experimental conditions.

In the pressure RAO results from the simulations, two distinct peaks are observed: one associated with the pumping mode of the pressure surfaces, and another corresponding to the heave resonance. However, these peaks are not evident in the experimental results, and the simulated pressure RAOs are notably higher than the experimental values in short waves within the range $\lambda_w/L \in [0.6\ 1.6]$. In addition, no clear peak appears at the natural frequency of heave, which is unexpected given that pronounced heave resonance is observed in the free decay tests, as shown in Fig. 12. This discrepancy suggests that the absence of corresponding peaks in both the heave motion and pressure RAOs is not physically consistent and warrants further investigation. Possible contributing factors include nonlinear effects such as damping pool dynamics and aerodynamic damping on the pressure surfaces, which may enhance energy dissipation in practice. Additionally, towing-induced forward tilt of the floating body alters the hydrostatic balance—raising the equilibrium pressure in the front bucket—and may lead

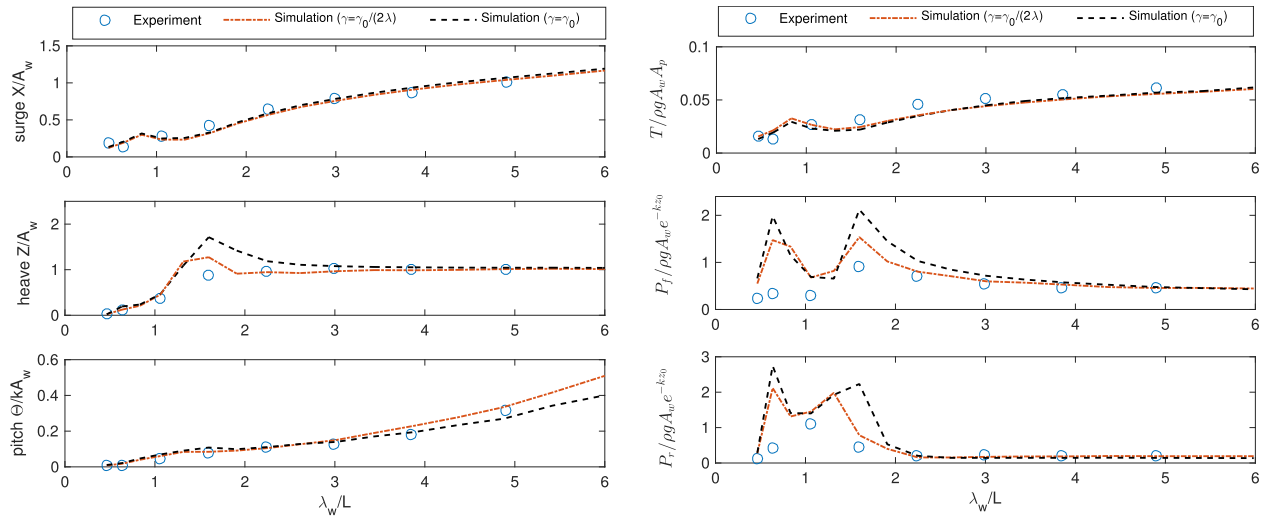

Fig. 15. Comparison of the towing system response in regular waves. Left: motion RAOs in surge, heave, and pitch. Right: RAOs for towing force, front bucket pressure, and rear bucket pressure. here, A_w denotes the wave amplitude, λ_w the wavelength, A_p the projected area, and z_0 the still water level of the pressure surfaces.

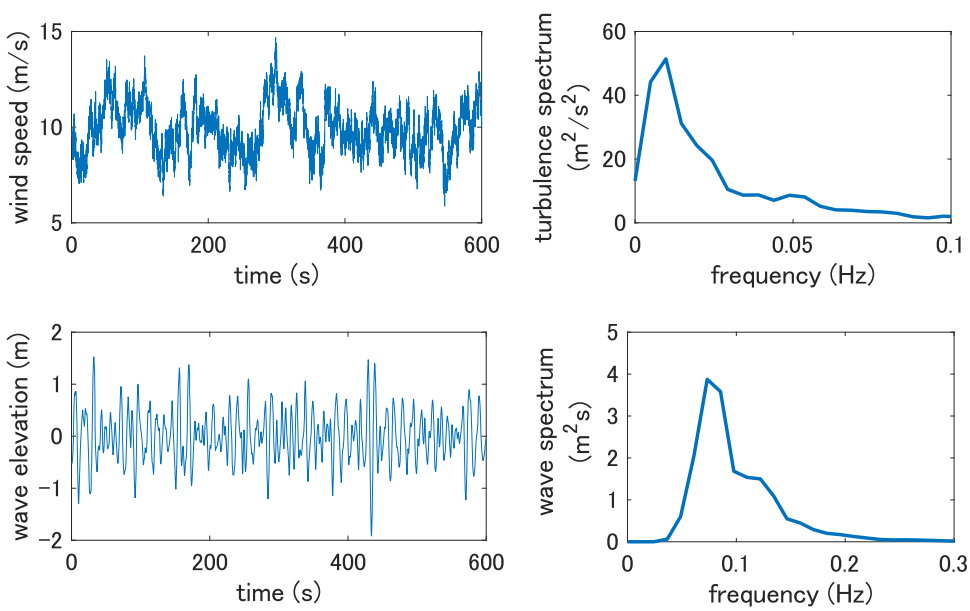

Fig. 16. Wind speeds at hub height and wave elevation at the origin of Global coordinate frame in the first 10 min.

to asymmetric pressure responses between the front and rear suction caissons.

4.3. Towing with circular route

A circular towing route with a radius of 500 m is studied to investigate the dynamics of the towing system under various met-ocean conditions. The configuration allows systematic evaluation of the response of the system to different incident directions of wind, waves, and current along the route. The use of a circular path enables efficient assessment of directional sensitivity without requiring multiple separate simulations. The trajectory of the towing tugboat is shown as the dashed line in Fig. 17(a). The towing operation starts on the west side and proceeds clockwise at a constant speed of 2 m/s. Waves propagate from North to South, while winds and current are both set to flow from West to East, creating a misalignment between wind and wave directions. This setup is particularly important, as the towing force may decrease significantly when the towing direction aligns with the wind and current, potentially degrading the course stability performance of the towing system. The selected route thus provides a comprehensive means to examine performance under realistic and variable environmental conditions.

A fully developed sea state characterized by the Modified Pierson-Moskowitz (MPM) Spectrum (Fossen, 2011)

$$S(\omega) = A_s \omega^{-5} \exp(-B_s \omega^{-4}) \tag{24}$$

is applied in this study. The terms A_s and B_s are the parameters given by

$$A_s = \frac{4\pi^3 H_s^2}{T_z^4}, \quad B_s = \frac{16\pi^3}{T_z^4}, \tag{25}$$

where H_s is the significant wave height set as $H_s = 2$ m, and T_z the zero-crossing period assigned by $T_z = 9$ s.

A moderate sea condition with a 1-h averaged wind speed of 10 m/s is considered, as it represents typical offshore operating conditions where both aerodynamic and hydrodynamic effects are significant but not extreme. The turbulence intensity is specified according to the IEC

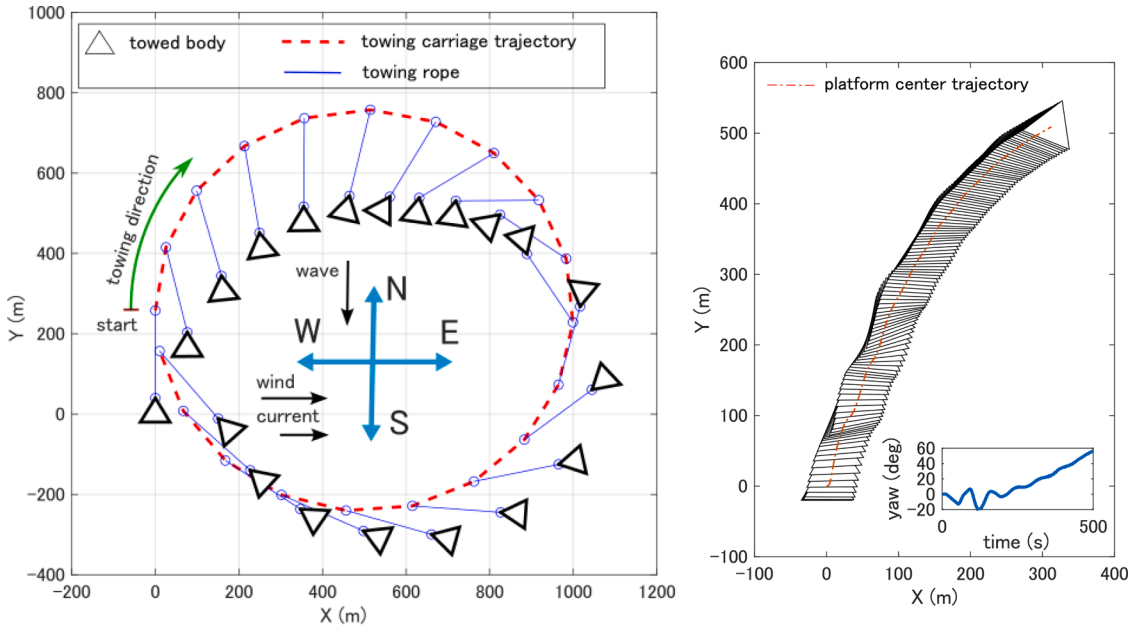

(a) (b)

Fig. 17. Motion trajectory of the towing system. (a) Results at 80-s interval; (b) Results at 3-s interval during the first 500 s.

Edition 2 standard (Burton et al., 2011):

$$I_u = I_{\text{ref}}\left(0.75 + \frac{5.6}{U_\infty(z_h)}\right), \tag{26}$$

where the reference turbulence intensity is given by $I_{\text{ref}} = 0.14$. The time-series wind speed and wave elevation for the first 10 min, along with their respective spectra, are presented in Fig. 16. In the simulation, the wind field is assumed to be spatially uniform, meaning that wind speed does not vary with location during the towing process. TurbSim (Jonkman, 2014) is used to generate time-series wind speed data, and the aerodynamic loads on the wind turbine are computed using the quasi-steady aerodynamic model, based on instantaneous relative wind speeds and lift/drag coefficients by (3) and (4).

The current is assumed to be uniform with a speed of 1 m/s. Based on these environmental settings, simulations are carried out and the trajectory of the platform, including the position and the orientation at 80-s

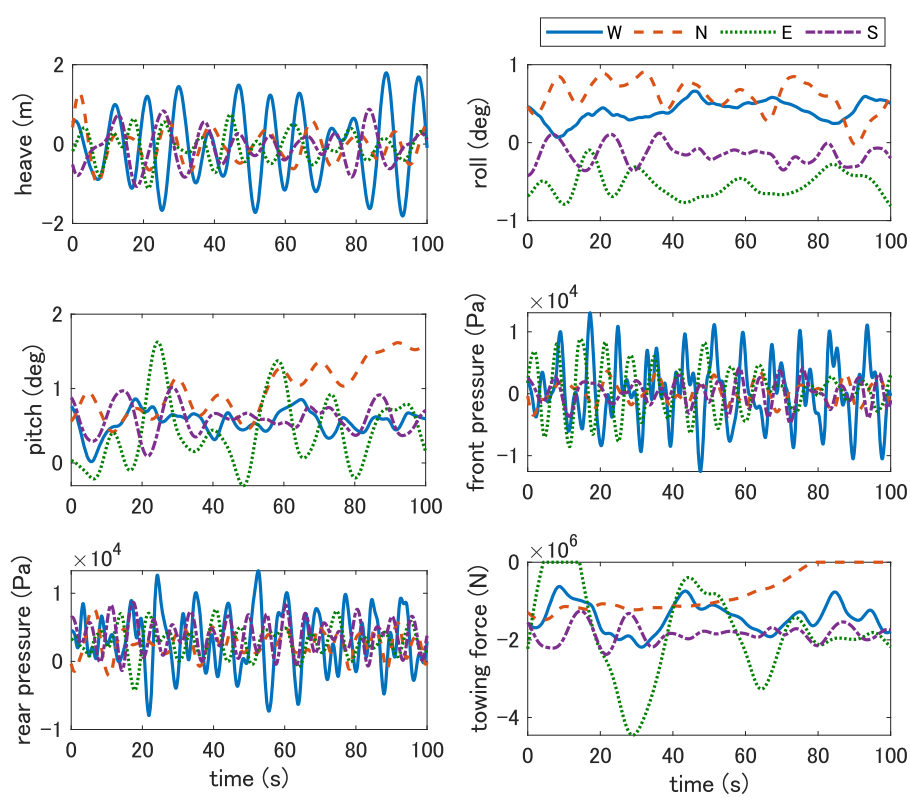

Fig. 18. Comparison of the platform motion in heave, roll, and pitch, the pressures in buckets, and the towing force at the Northwest, Northeast, Southeast, and Southwest sides.

interval, is shown in Fig. 17(a). Owing to the thrust generated by winds and current, the platform follows an elliptical path rather than a perfect circle. The maneuvering behavior of the platform during the first 500 s is illustrated in Fig. 17(b). It is observed that during the initial transient phase, the towed body exhibits oscillatory motion in its course, which gradually converges, indicating that the towing operation maintains course stability under the given met-ocean conditions.

The platform motion in heave, roll, and pitch, the pressures in the front bucket and one of the rear buckets, as well as the towing force at the West, North, East, and South positions along the circular route, are shown in Fig. 18. To eliminate the influence of the initial transient phase, the results from the second full rotation of the circular towing path are presented. At the West position, the heave motion and caisson pressures exhibit the largest fluctuations, as the encounter wave frequencies closely match their natural frequencies. Moreover, large-amplitude oscillations in the towing force are observed at the North and East positions, where the force occasionally drops to zero. This behavior can be attributed to the wind and current loads acting predominantly on the lateral sides of the towed body, perpendicular to the towing direction. Due to the strong coupling between towing force and pitch motion, the pitch exhibits larger fluctuations at the North and East positions compared to other segments of the route. These findings highlight that the dynamic response of the towing system can vary substantially with changing sea directions. In extreme cases, such variations may even lead to a loss of control over the towed body. Therefore, route planning and towing speed optimization based on prevailing met-ocean conditions are essential for safe and efficient towing operations.

5. Conclusion

In this study, a wet towing system was developed for a multi-bucket jacket foundation wind turbine and evaluated through wave basin experiments and numerical simulations. Experimental tests using a scaled model were conducted to investigate the dynamic characteristics of the system. A coupled aero-hydro-towing numerical model was developed in Simulink, incorporating the effects of air compressibility within the suction caissons. Linear and nonlinear damping coefficients were estimated based on experimental measurements. The good agreement between experimental and simulation results validates both the parameter estimation approach and the reliability of the numerical model.

To explore the system behavior under realistic conditions, a circular towing route was simulated, allowing analysis of system responses under varying met-ocean environments. Based on the findings, several important considerations are identified for future research:

- Pneumatic compressibility in the caissons not only weakens the restoring capability but also alters damping characteristics. Specifically, natural frequencies in the vertical directions are reduced by approximately 3.5 %, while the damping factor decreases by 16 % in heave and increases by 25 % in pitch.
- Caution is needed regarding scale effects introduced by suction caissons in physical model tests. To preserve dynamic similarity, the heat capacity ratio in the numerical model should be adjusted appropriately.
- The proximity of the natural frequencies of the platform and pressure surfaces to the wave excitation frequencies may lead to resonance under heading wave conditions. Towing route optimization is critical to enhance operational reliability.

Overall, this study presents a fast and practical simulation framework for evaluating wet towing systems in realistic seaway conditions. Future work will focus on developing path-following control strategies to further improve towing performance and robustness.

Declaration of competing interest

The authors declare the following financial interests/personal relationships which may be considered as potential competing interests:

Changhong Hu reports financial support was provided by Ohbayashi Corporation. If there are other authors, they declare that they have no known competing financial interests or personal relationships that could have appeared to influence the work reported in this paper.

CRediT authorship contribution statement

Hongzhong Zhu: Writing – original draft, Visualization, Validation, Software, Resources, Methodology, Investigation, Formal analysis, Data curation; **Changhong Hu:** Writing – review & editing, Project administration, Conceptualization; **Seiya Watanabe:** Investigation, Conceptualization; **Makoto Sueyoshi:** Methodology, Investigation, Conceptualization; **Rikizo Yamashita:** Investigation, Funding acquisition, Conceptualization; **Yoshihiro Matsuoka:** Funding acquisition, Conceptualization.

Acknowledgments

This research was partly funded by a joint research project between Kyushu University and Obayashi Corporation in FY2023.

References

Aubault, A., Alves, M., Sarmento, A.n., Roddier, D., Peiffer, A., 2011. Modeling of an oscillating water column on the floating foundation windfloat. In: International Conference on Offshore Mechanics and Arctic Engineering. Vol. 44373, pp. 235–246.

Bagheri, P., Yoon, J.C., Park, D., Kim, J.M., 2019. Numerical analysis of suction bucket foundations used for offshore wind turbines. In: Proceedings of the 1st Vietnam Symposium on Advances in Offshore Engineering: Energy and Geotechnics. Springer, pp. 336–341.

Burton, T., Jenkins, N., Sharpe, D., Bossanyi, E., 2011. Wind Energy Handbook. New York: Wiley. second ed.

Chan, H., Xu, Z., Huang, W.L., 1995. Estimation of nonlinear damping coefficients from large-amplitude ship rolling motions. Appl. Ocean Res. 17 (4), 217–224.

Chuang, T.-C., Yang, W.-H., Yang, R.-Y., 2021. Experimental and numerical study of a barge-type FOWT platform under wind and wave load. Ocean Eng. 230, 109015.

Díaz, H., Soares, C.G., 2020. Review of the current status, technology and future trends of offshore wind farms. Ocean Eng. 209, 107381.

Falcão, A. F.O., Henriques, J. C.C., 2019. The spring-like air compressibility effect in oscillating-water-column wave energy converters: review and analyses. Renew. Sustain. Energy Rev. 112, 483–498.

Fossen, T.I., 2011. Handbook of Marine Craft Hydrodynamics and Motion Control. John Wiley & Sons.

Fujino, T., Hu, C., Watanabe, S., Tan, L., Yamashita, R., 2023. An experiment on wet-towing performance of a skirt suction offshore wind turbine foundation. In: In Proceedings of The Japan Society of Naval Architects and Ocean Engineers (JASNAOE), 37. The Japan Society of Naval Architects and Ocean Engineers (JASNAOE), pp. 459–462.

Gaertner, E., Rinker, J., Sethuraman, L., Zahle, F., Anderson, B., Barter, G., Abbas, N., Meng, F., Bortolotti, P., Skrzypinski, W., Scott, G., Feil, R., Bredmose, H., Dykes, K., Sheilds, M., Allen, C., Viselli, A., 2020. Definition of the IEA 15-Megawatt Offshore Reference Wind Turbine. Technical Report. International Energy Agency. https://www.nrel.gov/docs/fy20osti/75698.pdf.

Grecu, S., Barari, A., Ibsen, L.B., 2024. Key trends in the response of suction bucket foundations to extreme axial cyclic loads. Soil Dyn. Earthq. Eng. 176, 108344.

Ikoma, T., Tan, L., Moritsu, S., Aida, Y., Masuda, K., 2021. Motion characteristics of a barge-type floating vertical-axis wind turbine with moonpools. Ocean Eng. 230, 109006.

Jonkman, B.J., 2014. Turbsim user's guide v2. 00.

Lee, C.H., Newman, J.N., 2016. WAMIT User Manual, Version 7.4. WAMIT, Inc., Chestnut Hill, MA.

Li, J., Lian, J., Guo, Y., Wang, H., 2024. Concept design and floating installation method study of multi-bucket foundation floating platform for offshore wind turbines. Mar. struct. 93, 103541.

Lian, J., Li, J., Guo, Y., Wang, H., Yang, X., 2022. Numerical study on local scour characteristics of multi-bucket jacket foundation considering exposed height. Appl. Ocean Res. 121, 103092.

Lian, J., Xiao, T., Liu, D., Ye, F., Xiong, D., 2023. The offshore prefabrication and semi-wet towing of a bucket foundation for offshore wind turbines. Ocean Eng. 285, 115354.

MathWorks, 2024. Simscape multibody user's guide. https://www.mathworks.com/products/simscape-multibody.html. [accessed on 11/August/2024].

Mauro, F., Nabergoj, R., 2021. Determination of ship roll damping coefficients by a differential evolution algorithm. In: Journal of Physics: Conference Series. Vol. 2090. IOP Publishing, p. 012135.

McCoy, A., Musial, W., Hammond, R., Mulas Hernando, D., Duffy, P., Beiter, P., Perez, P., Baranowski, R., Reber, G., Spitsen, P., 2024. Offshore Wind Market Report: 2024 Edition. Technical Report. National Renewable Energy Laboratory (NREL), Golden, CO (United States).

Shonberg, A., Harte, M., Aghakouchak, A., Brown, C., Andrade, M.P., Liingaard, M.A., 2017. Suction bucket jackets for offshore wind turbines: applications from in situ observations. In: Proc. TC209 Workshop, 19th International Conference on Soil Mechanics and Geotechnical Engineering, Seoul, South Korea, pp. 65–77.

Tan, L., Hu, C., Liu, Y., 2023. Numerical simulations of towing a jacket foundation with triple buckets. In: IOP Conference Series: Materials Science and Engineering. Vol. 1288. IOP Publishing, p. 012033.

Wang, L., Robertson, A., Jonkman, J., Kim, J., Shen, Z.-R., Koop, A., Borràs Nadal, A., Shi, W., Zeng, X., Ransley, E., et al., 2022. OC6 phase ia: CFD simulations of the free-decay motion of the deepcwind semisubmersible. Energies 15 (1), 389.

Wei, X., Wang, T., Wang, Y., Liu, Y., Jiang, M., Zhang, P., 2025. Horizontal bearing performance of the four-bucket jacket foundation. J. Marine Sci. Appl., 24, 542–551.

Yasukawa, H., Yoshimura, Y., 2015. Introduction of MMG standard method for ship maneuvering predictions. J. Mar. Sci. Technol. 20 (1), 37–52.

Zhang, P., Ding, H., Le, C., Huang, X., 2013. Motion analysis on integrated transportation technique for offshore wind turbines. J. Renew. Sustain. Energy 5 (5).

Zhang, P., Ding, H., Le, C., et al., 2022. Response analysis of a lowering operation for a three-bucket jacket foundation for offshore wind turbines. Renew. Energy 185, 564–584.